Structural and Electrochemical Characterization of Thin Film Li_2MoO_3 Electrodes

Ethan C. Self[1z], Yiman Zhang[1], Andrew K. Kercher[1], Nathan D. Phillip[2], Frank M. Delnick[1], Jagjit Nanda[1z]

[1]Chemical Sciences Division, Oak Ridge National Laboratory, Oak Ridge, TN, 37831, USA
[2]The Bredesen Center for Interdisciplinary Research and Graduate Education, University of Tennessee, Knoxville, TN, 37996, USA

[z]Corresponding Author E-mail Addresses: E. C. Self selfec@ornl.gov
J. Nanda nandaj@ornl.gov

Abstract

Li_2MoO_3 is a promising structural stabilizing unit for use in composite layered-layered cathodes for Li-ion batteries. To enable the rational design of such cathodes, studies on fundamental phenomena related to the active material structure and electrode/electrolyte interface are needed. The present work details the fabrication and characterization of thin film Li_2MoO_3 cathodes and shows that their electrochemical performance greatly depends on the nature of the cathode/electrolyte interface. The Li_2MoO_3 thin films exhibit poor cyclability in a liquid carbonate electrolyte (e.g., initial capacity of 166 mAh/g with 40% capacity fade over 20 cycles) whereas all-solid-state Li_2MoO_3/Lipon/Li batteries show negligible fade during cycling. A suite of characterization methods including Raman spectroscopy and X-ray photoelectron spectroscopy are used to study the evolution of the cathode structure and cathode electrolyte interphase (CEI) layer during charge/discharge cycling. Li transport rates are another important factor which affect cathode performance. AC impedance spectroscopy studies reveal that the Li diffusion coefficient (D_{Li}) in Li_2MoO_3 decreases from 4.36 x 10^{-11} cm^2/s in the fully discharged state to 4.51 x 10^{-13} cm^2/s when charged to 3.6 V vs. Li/Li^+. Overall, the results presented herein provide insight on the fundamental phenomena which govern Li_2MoO_3 cathode performance.

Introduction

A battery's performance is governed by phenomena occurring at the electrode/electrolyte interfaces. These interfaces oftentimes evolve during battery operation due to: (i) electrode volume changes, (ii) active material phase transformations, and/or (iii) electrolyte decomposition on the electrode surface. For Li-ion batteries (LIBs), the structure and composition of the solid-electrolyte interphase (SEI) layer comprised of electrolyte reduction products has been extensively studied for many anode materials including graphite, Si, and Ge.(1-5) However, comparatively little work has been conducted on the analogous cathode electrolyte interphase (CEI) layer which depends on many factors including electrolyte composition, cathode chemistry, and cycling protocol.(6-8) Fundamental studies on the cathode/electrolyte interface are thus needed to guide development of high voltage LIB cathodes.

When charged beyond 4.3 V vs. Li/Li^+, most lithium transition metal oxide cathodes (e.g., $LiMO_2$, M = Ni, Mn, Co) are structurally unstable, resulting in irreversible capacity loss and voltage fade during cycling. One approach to improve cathode stability at high states-of-charge is to integrate LiM^IO_2 (for Li storage) with $Li_2M^{II}O_3$ moieties (for structural stability). Examples of these composite layered-layered systems include Li-Mn-rich NMC (xLi_2MnO_3•$(1-x)LiNi_xMn_yCo_{1-x-y}O_2$)(9-12) and a Mo-containing analogue (xLi_2MoO_3•$(1-x)LiNi_xMn_yCo_{1-x-y}O_2$).(13) Unlike Li_2MnO_3 which irreversibly evolves Li_2O during the formation cycle, Li_2MoO_3 possesses a stable oxygen framework (up to 4.8 V vs. Li/Li^+) and can reversibly cycle 1 Li per formula unit. Thus, Li_2MoO_3 can potentially serve as an electrochemically active structural stabilizer in LIB cathodes.

To aid the development of these new Mo-containing cathodes, phenomena occurring at the cathode/electrolyte interface during battery operation (e.g., Li transport, charge transfer, electrolyte decomposition, etc.) must be well-understood. However, interpreting *in-situ* and *ex-situ* data collected with conventional slurry cast electrodes is oftentimes complicated by the presence of conductive carbon and polymer binder which may participate in side reactions with the electrolyte and/or produce signals that overlap with the desired signal from the active material. To resolve this issue, radio frequency (RF) magnetron sputtered thin film cathodes composed entirely of active material represent a model system to study new cathode chemistries. In addition to eliminating unwanted signal arising from inactive components, sputtered thin films have a planar surface (as opposed to the complex pore structure of slurry cast electrodes) which greatly facilitates interpretation of AC impedance spectroscopy data. Finally, thin film cathodes can be readily interfaced with oxidatively stable solid electrolytes such as lithium phosphorus oxynitride (Lipon) in all-solid-state devices.(14-17)

The work herein details the preparation and characterization of thin film Li_2MoO_3 cathodes cycled in cells containing either a liquid carbonate electrolyte or in all solid-state Li_2MoO_3/Lipon/Li batteries. The structure and electrochemical properties of these thin films are compared with that of previously reported slurry cast Li_2MoO_3 cathodes.(13, 18-20) The CEI layer formed when cycling Li_2MoO_3 in a liquid electrolyte is characterized using *ex-situ* X-ray photoelectron spectroscopy (XPS). Finally, AC impedance spectroscopy is used to quantify Li transport rates in Li_2MoO_3 at various states-of-charge. Overall, these results represent a thorough investigation of thin film Li_2MoO_3 cathodes and provide insights on the phenomena which govern their performance.

Experimental

Li_2MoO_3 Thin Film Cathode Synthesis

Li_2MoO_3 was synthesized by reducing Li_2MoO_4 powder (Sigma-Aldrich, 99.9%) under flowing Ar/H_2 (96/4) at 675 °C for 72 h. A sputtering target was prepared by cold-pressing the Li_2MoO_3 powder into a pellet (54 mm diameter, 5 mm thick) at 19 MPa using a hydraulic press. The pellet was sintered at 650 °C under flowing Ar/H_2 (96/4). After sputtering bond layers of Cr, Ni, and then Au, the pellet was indium-bonded to a Cu backing plate. Thin film cathodes were fabricated on an Al_2O_3 substrate (1 mm thick) by first sputtering a Pt current collector layer (0.2 µm thick, DC sputtered at 10 W) followed by a Li_2MoO_3 cathode layer (1.23 µm thick). All-solid-state batteries were prepared using a 1 cm^2 cathode area deposited on a rectangular Pt/Al_2O_3 substrate. For tests with liquid electrolyte, the Li_2MoO_3 thin film was deposited on one side of a Pt/Al_2O_3 disc (1 cm diameter). The Li_2MoO_3 thin films were RF sputtered at 60 W at a working pressure of 20 mTorr Ar (~3.4 nm/min deposition rate) and were thermally annealed for 2 h at 650 °C under flowing Ar/H_2 (96/4). The morphology of the thin film Li_2MoO_3 cathodes was evaluated using scanning electron microscopy (SEM) conducted on a Zeiss Merlin SEM using an accelerating voltage of 1.00 – 20.00 kV.

Battery Fabrication

Li/Li_2MoO_3 batteries were prepared with either a liquid electrolyte (1.2 M $LiPF_6$ in ethylene carbonate/ethyl methyl carbonate (EC/EMC), 3/7 by weight) or solid electrolyte (Lipon). For the liquid system, CR2032 half cells were constructed in an Ar-filled glovebox using a Li_2MoO_3 thin film cathode and a Li metal counter/reference electrode (750 µm thick).

The separator consisted of one sheet of Celgard 2325 and one sheet of glass microfiber (Whatman DBS 30). For the all solid-state batteries, a 1.5 μm Lipon layer was magnetron sputtered at 75 W under flowing N_2 (20 sccm) on top of a thermally-annealed Li_2MoO_3 thin film (1 cm^2 active layer sputtered onto a rectangular Al_2O_3 substrate). Finally, Li metal (ca. 3 μm thick) was vapor deposited on the Lipon layer to form an all-solid-state battery. To avoid air exposure during electrochemical characterization, the all-solid-state batteries were hermetically sealed in stainless steel jars containing electrical leads in an Ar-filled glovebox.

Electrochemical Characterization

Galvanostatic charge/discharge experiments were conducted by polarizing cells between 2.0 – 4.8 V at current densities ranging from 10 – 12 $\mu A/cm^2$ using a MACCOR Series 4000 battery tester. All cycling experiments were performed at room temperature (ca. 23 °C). AC impedance spectra for the solid-state devices were acquired in a temperature-controlled chamber at 80 °C with a 10 mV AC perturbation over the frequency range $6.8 \times 10^5 – 1 \times 10^{-4}$ Hz using a Bio-Logic SP-200 potentiostat/galvanostat.

Electrodes for post-mortem analysis were harvested from cycled coin cells which were disassembled inside an Ar-filled glovebox. The electrodes were rinsed several times with dimethyl carbonate and dried under vacuum overnight without exposure to ambient conditions.

Raman Spectroscopy

Li_2MoO_3 cathodes were hermetically sealed in an optical cell (EL-Cell) in an Ar-filled glovebox to avoid air exposure. Raman spectra were acquired with an Alpha 300 confocal

Raman microscope (WITec, GmbH) using a solid-state 532 nm excitation laser, a 20× objective lens, and a grating with 600 grooves per mm. The laser spot size and power were approximately 1 μm and 100 μW, respectively. Raman spectra were analyzed using WITec Project Plus software. Representative spectra collected over a large electrode area (at least 50 × 50 um^2) are reported.

X-ray Diffraction (XRD)

XRD measurements on Li_2MoO_3 thin films were performed on a Scintag XDS 2000 powder diffractometer with Cu Kα radiation (λ = 1.540562 Å) in the 2θ range of 10 − 80°. The operating voltage and current of the X-ray generator were 45 kV and 35 mA, respectively.

X-ray Photoelectron Spectroscopy (XPS)

X-ray photoelectron spectroscopy (XPS) measurements were collected on a PHI 3056 XPS spectrometer operated at 350 W and 15 kV with a Mg Kα source (1253.6 eV). To avoid air exposure, samples were transferred under vacuum from an Ar-filled glove box to a cryo-pumped vacuum chamber operated at $<10^{-9}$ Torr (10^{-11} Torr base pressure) for measurement. Survey scans were collected at 93.9 eV pass energy with 0.5 eV energy steps while high resolution scans were acquired at 23.5 eV pass energy and 0.05 eV energy steps with 20 – 60 repeats for all spectra to improve the signal-to-noise ratio. Spectra were shifted relative to the adventitious carbon peak (284.8 eV) to correct for charging.

Results and Discussion

Figure 1 shows scanning electron microscopy (SEM) images of Li_2MoO_3 thin films deposited on a substrate consisting of a Pt current collector and an Al_2O_3 support. The thin film's surface (Figure 1a) contained irregular features on the order of 1 μm in size. Nonetheless, the film was reasonably smooth as indicated by the cross-sectional SEM image shown in Figure 1b. The average film thickness was 1.23 μm based on the deposition rate (~3.4 nm/min) measured using a quartz crystal microbalance present in the sputtering chamber.

Figure 2a shows an X-ray diffraction (XRD) pattern of a pristine Li_2MoO_3 thin film cathode. Most of the diffraction peaks are attributed to the underlying substrate, and only weak peaks assigned to Li_2MoO_3 were observed. Interestingly, the thin film showed some crystallographic texturing where certain planes were preferentially deposited during sputtering. For example, in Figure 2a the strongest Li_2MoO_3 reflection was from the (1 0 1) crystallographic plane, but the (0 0 3) plane is most intense for polycrystalline Li_2MoO_3 with random crystallite orientation.(13) The formation of anisotropic crystallographic orientations is a complex phenomenon which is influenced by the substrate, sputtering conditions, and mechanical stresses in the film. This texturing effect has been reported for various metal oxide films prepared by magnetron sputtering(21-23), but a mechanistic understanding of the crystallographic orientation observed here is beyond the scope of this study. The Li_2MoO_3 thin film's structure was also analyzed using Raman spectroscopy as shown in Figure 2b. The bands located at 275, 372, and 931 cm^{-1} are assigned to Mo=O vibrational modes, and the bands at 494 and 732 cm^{-1} are due to symmetric and antisymmetric Mo-O-Mo stretches, respectively.(24, 25) While these band positions were well-matched to Li_2MoO_3, the relative

intensity of the thin film's bands differed from those of the Li_2MoO_3 powder, likely due to the texturing effect previously mentioned. Nonetheless, the lack of additional Raman bands indicates the thin film contained no detectable phase impurities. Furthermore, the Raman spectra were extremely uniform with negligible variation over a large area (50 x 50 μm^2 with 1 μm^2 resolution) which indicates the presence of a high-quality cathode layer suitable for electrochemical characterization.

The electrochemical properties of the Li_2MoO_3 thin film cathodes were first evaluated in coin cells using a liquid electrolyte (1.2M $LiPF_6$ EC+EMC) and Li metal anode. The open-circuit potential of freshly assembled cells ranged from 2.4 – 2.6 V which is in good agreement with previous studies on Li_2MoO_3.(13, 18-20) During the first charging step (Figure 3a), the cathode showed two plateaus near 2.6 and 3.6 V vs. Li/Li^+ with a total capacity of 195 mAh/g (corresponding to formation of $Li_{0.85}MoO_3$). Upon discharge, the cathode exhibited a sloping profile with an initial reversible capacity of 166 mAh/g (ca. 1 Li cycled per formula unit) which faded to 99 mAh/g after 20 cycles. Most of the charge compensation occurred ~2.0 – 3.5 V vs. Li/Li^+ due to the reversible Mo^{4+}– Mo^{6+} redox center, but irreversible oxidation processes were also observed at potentials near 3.7 V vs. Li/Li^+ throughout the first 20 cycles. These features (shown more clearly on the differential capacity plots in Figure 3b) are possibly due to oxidation of Li_2CO_3 on the cathode surface(26) as described by Equation 1:

$$2\ Li_2CO_3 \rightarrow 4\ Li^+ + 4\ e^- + 2CO_2 + O_2,\ E^0 = 3.82\ V\ vs.\ Li/Li^+ \quad (1)$$

This conclusion is consistent with XPS results (discussed later in the text) which show the Li_2CO_3 surface layer is removed during cycling.

The voltage profile during the first charging step in Figure 3a was significantly different

from that of subsequent cycles which suggests that the Li_2MoO_3 may have undergone an irreversible structural rearrangement. Thus, *ex-situ* Raman spectroscopy was used to evaluate the structure of Li_2MoO_3 at different states-of-charge and cycling history (see Figure 4). Compared to the pristine cathode, the cycled thin films exhibited significantly broader Raman bands whose positions shifted slightly throughout the first cycle. After 20 cycles, the Raman spectrum contained two very broad, convoluted bands located at 100 – 600 and 800 – 1000 cm^{-1}. This band broadening is due to a loss of symmetry in the $Li_{2-x}MoO_3$ structure and indicates an irreversible crystalline to amorphous transformation occurred during cycling.(13)

In addition to changes in the bulk structure of Li_2MoO_3, the cathode surface chemistry also evolved during cycling due to accumulation of electrolyte decomposition products. X-ray photoelectron spectroscopy (XPS) was used to study changes in the cathode surface when cycled in the liquid electrolyte. Figure 5a shows the Mo 3d core level spectra of Li_2MoO_3 powder and thin film cathodes at the following conditions: (i) pristine (i.e., uncycled), (ii) after 1 cycle (discharged to 2.0 V), and (iii) after 20 cycles (discharged to 2.0 V). The spectra were fit with four peaks associated with the $3d_{5/2}$ and $3d_{3/2}$ orbitals for Mo^{6+} and Mo^{4+}.(27, 28) The XPS data showed substantial amounts of Mo^{6+} were present in the pristine Li_2MoO_3 powder and thin film, indicating partial oxidation of Li_2MoO_3 to Li_2MoO_4 and/or MoO_3 near the surface during sample preparation.(29) Compared to pristine Li_2MoO_3, the cycled electrodes showed significant band broadening with convolution of the $3d_{5/2}$ and $3d_{3/2}$ peaks. This result indicates the presence of diverse Mo bonding environments due to cycling-induced amorphization as previously discussed. Furthermore, the Mo 3d signal was of much lower

intensity (and therefore noisier) after 20 cycles due to formation of a CEI layer on the cathode surface.

Analysis of the O 1s and C 1s core level scans (Figures 5b and 5c) provides further insight to the cathode surface chemistry before and after electrochemical cycling.(6, 30) The O 1s scans for the pristine powder and thin film were nearly identical and showed a broad peak ranging from 528 – 535 eV. The signal near 530 eV is attributed to metal-oxygen bonding (e.g., Mo-O), whereas the signal at higher energies suggests the presence of some organic C-O and/or C=O species (e.g., Li_2CO_3) formed during sample preparation.(6, 31) The presence of Li_2CO_3 on the pristine cathode was supported by the C 1s peak at 290 eV (Figure 5c). After electrochemical cycling, dramatic changes in the cathode's surface chemistry were observed. Notably, the cycled samples contained very little Li_2CO_3 at the surface (as evidenced by the weakened peak at 290 eV), indicating that Li_2CO_3 was consumed during electrochemical cycling as previously discussed. The O 1s peak in the cycled samples contained weaker signals from Mo-O (represented by the blue peak near 530 eV) due to growth of the CEI layer. Figure 5c indicates the CEI layer contained organic compounds with C-C, C-H, and C-O functionalities, possibly due to the formation of poly(ethylene oxide)-like species during decomposition of ethylene carbonate.(6, 8, 30)

The lack of a fluorine-containing polymer binder (e.g., poly(vinylidene fluoride), PVDF) in the thin film cathodes allows $LiPF_6$ decomposition products to be readily identified. The F 1s spectra shown in Figure 5d indicate that $LiPF_6$ decomposed on the cathode surface to form: (i) LiF (685 eV) after the 1st cycle and (ii) Li_xPF_y (688 eV) during extended cycling.(6, 30) The C 1s and O 1s peaks were also analyzed to determine F bonding environments in the CEI layer.

The lack of a peak at 293 eV in the C 1s spectra indicates the CEI layer did not contain any C-F moieties, while the growing shoulder at 534 eV in the O 1s spectra is attributed to the accumulation of O-F_x products. Overall, the results in Figure 5 provide information on the qualitative chemical functionality of the CEI layer formed when cycling Li_2MoO_3 in a liquid carbonate electrolyte.

In addition to experiments using conventional liquid carbonate electrolytes, all-solid-state Li/Li_2MoO_3 cells containing a lithium phosphorus oxynitride (Lipon) solid electrolyte were fabricated and tested. Due to its excellent oxidative stability, Lipon is a particularly useful electrolyte for high voltage cathode materials operated at very positive electrochemical potentials.(15, 16) The cycling profiles of a Li_2MoO_3/Lipon/Li thin film battery (Figure 6a) exhibited a sloping profile with most of the charge compensation occurring at 2.0 – 3.5 V vs. Li/Li^+. Interestingly, the corresponding differential capacity plots (Figure 6b) for the solid-state battery differed from those obtained when cycling Li_2MoO_3 in a liquid electrolyte. The irreversible peak near 3.7 V vs. Li/Li^+ observed in the liquid electrolyte system (attributed to oxidation of Li_2CO_3) was absent in the solid-state device. Possible explanations for this behavior include: (i) changes in the Li_2MoO_3 thin film surface chemistry may have occurred when sputtering the Lipon layer, and/or (ii) Li_2CO_3 oxidation may have been kinetically slower in the presence of the Lipon layer.

Previous studies have shown that interfacial chemical reactions may occur between the cathode and electrolyte in all-solid-state batteries.(32-34) For example, Wang et al.(32) reported that $LiCoO_2$ and Lipon spontaneously react to form a disordered layer containing Li_2O, Li_2O_2, and Co-based species. A detailed investigation of possible interfacial reaction layers in

Li_2MoO_3/Lipon/Li solid-state cells is beyond the scope of the present study. The formation of such interfacial layers does not necessarily degrade device performance, and Lipon coatings have been shown to improve the cycling stability of many high-voltage cathode systems including $Li_{1.2}Mn_{0.525}Ni_{0.175}Co_{0.1}O_2$(17) and $LiMn_{1.5}Ni_{0.5}O_4$.(35)

As shown in Figure 6c, the Li_2MoO_3/Lipon/Li thin film battery showed excellent cycling stability with an initial reversible capacity of 116 mAh/g and only 6.4% fade over 45 cycles which indicates the presence of a stabilized cathode/electrolyte interface. On the other hand, the cathode cycled in a liquid electrolyte exhibited increased voltage hysteresis during cycling and 40% capacity fade over 20 cycles (see Figure 3a). The poor performance of the liquid cell is attributed to accumulation of electrolyte decomposition products on the cathode surface which led to increased cell resistance during cycling. Overall, the results in Figures 3 and 6 demonstrate that the cathode's performance greatly depends on electrolyte selection and the nature of the cathode/electrolyte interface.

In addition to properties of the electrode/electrolyte interface, cathode performance is also influenced by Li transport rates in the active material which can be readily quantified using AC impedance spectroscopy. Whereas conventional slurry cast electrodes contain complex pore structures that affect the system's impedance, the planar geometry of thin film batteries greatly simplifies interpretation of impedance data. In particular, the Li diffusion coefficient in thin film cathodes can be determined from the slope of reactance (or resistance) plotted as a function of $\omega^{-1/2}$ over the appropriate frequency range as shown in Equations 2 and 3:

$$Z_w = A\omega^{-1/2} - jA\omega^{-1/2} \quad (2)$$

$$A = \left| \frac{V_m \left({}^{dE}/_{dy} \right)}{zFa\sqrt{2D_{Li}}} \right| \quad (3)$$

where Z_w (Ω) is the Warburg complex impedance element under semi-infinite diffusion boundary conditions, ω (s^{-1}) is the radial frequency of the AC perturbation, V_m ($cm^3\ mol^{-1}$) is the partial molar volume of the active material, dE/dy (V) is the slope of the coulombic titration curve, z is the molar equivalence (equal to 1 for Li), F is Faraday's constant (96,485 C mol^{-1}), a (cm^2) is the cathode/electrolyte interfacial area, and D_{Li} is the Li diffusion coefficient in the cathode ($cm^2\ s^{-1}$). A derivation of this relationship is given by Ho et al.(36)

AC impedance studies on a Li_2MoO_3/Lipon/Li thin film battery were performed at 80 °C to expedite data acquisition by: (i) reducing the time needed to reach near-equilibrium conditions and (ii) increasing the frequency range at which the semi-infinite diffusion boundary conditions specified by Ho et al.(36) were satisfied. To acquire the impedance spectra, the cell was galvanostatically charged/discharged at ± 5 μA/cm^2 followed by a potential hold until the absolute current density decayed below 0.05 μA/cm^2. Further potential holds did not notably impact the cell's impedance, indicating this protocol was adequate to analyze the system at near-equilibrium conditions. Figure 7 shows Nyquist plots for a Li_2MoO_3/Lipon/Li thin film battery acquired at various states-of-charge during discharging and charging steps. At intermediate frequencies (ca. 10 – 0.1 Hz), the Nyquist plots showed straight lines angled at approximately 45°, indicating semi-infinite diffusion was the dominant process in this regime. At the lowest frequencies (down to 1 x 10^{-4} Hz, see Figure 7c), capacitive tails arising from finite diffusion throughout cathode's thickness was observed. Theoretically, these lines should be perpendicular to the real axis, but the low frequency tails in Figure 7c are skewed due to

non-uniform current distribution, possibly caused by electrode roughness, nonuniform thickness, etc.

In the frequency range where semi-infinite diffusion boundary conditions were satisfied and thus Equation 2 was applicable (see Figure S1 for plots of Z_{real} vs. $\omega^{-1/2}$ and $-Z_{imaginary}$ vs. $\omega^{-1/2}$), D_{Li} in the thin film cathodes was calculated using Equation 3. These calculations were made with the following assumptions: (i) D_{Li} in the Li_2MoO_3 cathode was much lower than that in the Lipon electrolyte and Li anode, (ii) the cathode partial molar volume (V_m) was 32.2 cm^3/mol (calculated from the theoretical density and molecular weight of Li_2MoO_3) and was constant over the potential range investigated, and (iii) (dE/dy) values were obtained from a slow galvanostatic charge/discharge curve collected at 5 μA/cm^2 (see Figure S2). As shown in Figure 8, the measured D_{Li} in the fully discharged state (2.0 V vs. Li/Li^+) was 4.36 x 10^{-11} cm^2/s and decreased 2 orders of magnitude to 4.51 x 10^{-13} cm^2/s after charging to 3.6 V. D_{Li} gradually increased upon relithiation, indicating that Li transport rates in Li_2MoO_3 were generally faster at low states-of-charge. A mechanistic understanding of this behavior is beyond the scope of this work, but these results imply that the rate limiting step (e.g., Li transport vs. reaction kinetics) could change depending the cell's state-of-charge.

Conclusions

The present study details the structural and electrochemical characterization of Li_2MoO_3 thin film cathodes prepared using RF sputtering. When cycled in a liquid carbonate electrolyte, the cathodes exhibited an initial reversible capacity of 166 mAh/g which rapidly faded to 99

mAh/g after 20 cycles. In comparison, all-solid-state Li_2MoO_3/Lipon/Li thin film batteries showed excellent stability with negligible capacity fade over 45 cycles.

The discrepancies between devices containing liquid vs. solid electrolytes are attributed to differences in the cathode/electrolyte interface. *Ex-situ* XPS measurements showed that the carbonate electrolyte decomposed to form a CEI layer containing organic (C-O, C=O, C-C, C-H, and C-O) and inorganic (Li_xPF_y, LiF, O-F_x) species. Interestingly, the native Li_2CO_3 surface layer on the cathode surface was consumed during electrochemical cycling. Compared to the liquid electrolyte, the superior oxidative stability of Lipon enabled formation of a stable interface with Li_2MoO_3 even when charged to 4.8 V vs. Li/Li^+. These results suggest that interfacing with Lipon is a suitable approach to stabilize other high voltage cathode materials which operate outside the thermodynamic stability window of liquid electrolytes.

Unlike conventional slurry cast electrodes containing conductive carbon and polymer binder, thin film cathodes comprised entirely of active material enable one to readily probe the cathode structure and assess how the cathode/electrolyte interface evolves during cycling. Furthermore, the planar geometry of thin film cathodes greatly simplifies interpretation of AC impedance data to quantify Li transport rates as shown here. Overall, the present study demonstrates the advantages of a thin film cathode structure to study the fundamental phenomena which govern LIB cathode performance.

Acknowledgments

The authors thank Dr. Nancy J. Dudney and Dr. Gabriel M. Veith for their support with magnetron sputtering and XPS. We also thank Dr. Andrew S. Westover for assistance with the

solid-state Li_2MoO_3/Lipon/Li batteries, Dr. Dale K. Hensley for assistance with SEM imaging, and Dr. Harry M. Meyer III for fruitful discussions. Scanning electron microscopy was conducted at the Center for Nanophase Materials Sciences, which is a DOE Office of Science User Facility. This research was conducted at Oak Ridge National Laboratory, managed by UT Battelle, LLC, for the U.S. Department of Energy (DOE) under contract DE-AC05-00OR22725 and is sponsored by the Office of Energy Efficiency and Renewable Energy (EERE) Vehicle Technologies Office (VTO). The United States Government retains and the publisher, by accepting the article for publication, acknowledges that the United States Government retains a non-exclusive, paid-up, irrevocable, world-wide license to publish or reproduce the published form of this manuscript, or allow others to do so, for United States Government purposes. The Department of Energy will provide public access to these results of federally sponsored research in accordance with the DOE Public Access Plan (http://energy.gov/downloads/doe-public-access-plan).

References

1. S. J. An, J. Li, C. Daniel, D. Mohanty, S. Nagpure and D. L. W. III, *Carbon*, **105**, 52 (2016).
2. E. Peled and S. Menkin, *J. Electrochem. Soc.*, **164**, A1703 (2017).
3. A. Wang, S. Kadam, H. Li, S. Shi and Y. Qi, *Computational Materials*, **4**, 15 (2018).
4. E. Peled, *J. Electrochem. Soc.*, **126**, 2047 (1979).
5. X. L. Wu, Y. G. Guo and L. J. Wan, *Chem Asian J*, **8**, 1948 (2013).
6. K. Edström, T. Gustafsson and J. O. Thomas, *Electrochim. Acta*, **50**, 397 (2004).
7. W. Lu, J. Zhang, J. Xu, X. Wu and L. Chen, *ACS Appl. Mater. Interfaces*, **9**, 19313 (2017).
8. Y. M. Liu, G. N. B, J. L. Esbenshade and A. A. Gewirth, *Anal. Chem.*, **88**, 7171 (2016).
9. M. M. Thackeray, S.-H. Kang, C. S. Johnson, J. T. Vaughey, R. Benedek and S. A. Hackney, *J. Mater. Chem.*, **17**, 3112 (2007).
10. Y. Wu and A. Manthiram, *Electrochem. Solid-State Lett.*, **9**, A221 (2006).
11. S. Kim, M. Aykol, V. I. Hegde, Z. Lu, S. Kirklin, J. R. Croy, M. M. Thackeray and C. Wolverton, *Energy Environ. Sci.*, **10**, 2201 (2017).
12. S. K. K. S. K. Martha, *J. Electrochem. Soc.*, **165**, A463 (2018).
13. E. C. Self, L. Zou, M.-J. Zhang, R. Opfer, R. E. Ruther, G. M. Veith, B. Song, C. Wang, F. Wang, A. Huq and J. Nanda, *Chem. Mater.*, **30**, 5061 (2018).
14. J. B. Bates, N. J. Dudney, D. C. Lubben, G. R. Gruzalski, B. S. Kwak, X. Yu and R. A. Zuhr, *J. Power Sources*, **54**, 58 (1995).
15. N. J. Dudney, *Mater. Sci. Eng. B-Solid*, **116**, 245 (2005).
16. J. Li, C. Ma, M. Chi, C. Liang and N. J. Dudney, *Adv. Energy Mater.*, **5**, 1401408 (2015).
17. S. K. Martha, J. Nanda, Y. Kim, R. R. Unocic, S. Pannala and N. J. Dudney, *J. Mater. Chem. A*, **1**, 5587 (2013).
18. K.-S. Park, D. Im, A. Benayad, A. Dylla, K. J. Stevenson and J. B. Goodenough, *Chem. Mater.*, **24**, 2673 (2012).
19. A. C. W. P. James and J. B. Goodenough, *J. Solid State Chem.*, **76**, 87 (1988).
20. S. Kumakura, Y. Shirao, K. Kubota and S. Komaba, *PCCP*, **18**, 28556 (2016).
21. P. Thilakan, C. Minarini, S. Loreti and E. Terzini, *Thin Solid Films*, **388**, 34 (2001).
22. S. Mahieu, P. Ghekiere, D. Depla and R. De Gryse, *Thin Solid Films*, **515**, 1229 (2006).
23. A. S. Reddy, G. Venkata Rao, S. Uthanna and P. Sreedhara Reddy, *Physica B: Condensed Matter*, **370**, 29 (2005).
24. H. Jezlorowski and H. Knözinger, *The Journal of Physical Chemistry*, **83**, 1166 (1979).
25. H. Hu and I. E. Wachs, *The Journal of Physical Chemistry*, **99**, 10897 (1995).
26. N. Mahne, S. E. Renfrew, B. D. McCloskey and S. A. Freunberger, *Angew Chem Int Ed Engl*, **57**, 5529 (2018).
27. M. Zhang, G. Hu, L. Liang, Z. Peng, K. Du and Y. Cao, *J. Alloys Compd.*, **673**, 237 (2016).

28. Irfan, F. So and Y. Gao, *International Journal of Photoenergy*, 314702 (2011).
29. J. Ma, Y. Gao, Z. Wang and L. Chen, *J. Power Sources*, **258**, 314 (2014).
30. R. Dedryvère, S. Laruelle, S. Grugeon, L. Gireaud, J.-M. Tarascon and D. Gonbeau, *J. Electrochem. Soc.*, **152**, A689 (2005).
31. A. N. Mansour, *Surf. Sci. Spectra*, **3**, 279 (1996).
32. Z. Wang, D. Santhanagopalan, W. Zhang, F. Wang, H. L. Xin, K. He, J. Li, N. Dudney and Y. S. Meng, *Nano Lett.*, **16**, 3760 (2016).
33. K. H. Kim, Y. Iriyama, K. Yamamoto, S. Kumazaki, T. Asaka, K. Tanabe, C. A. J. Fisher, T. Hirayama, R. Murugan and Z. Ogumi, *J. Power Sources*, **196**, 764 (2011).
34. K. Park, B.-C. Yu, J.-W. Jung, Y. Li, W. Zhou, H. Gao, S. Son and J. B. Goodenough, *Chem. Mater.*, **28**, 8051 (2016).
35. Y. Kim, N. J. Dudney, M. Chi, S. K. Martha, J. Nanda, G. M. Veith and C. Liang, *J. Electrochem. Soc.*, **160**, A3113 (2013).
36. C. Ho, I. D. Raistrick and R. A. Huggins, *J. Electrochem. Soc.*, **127**, 343 (1980).

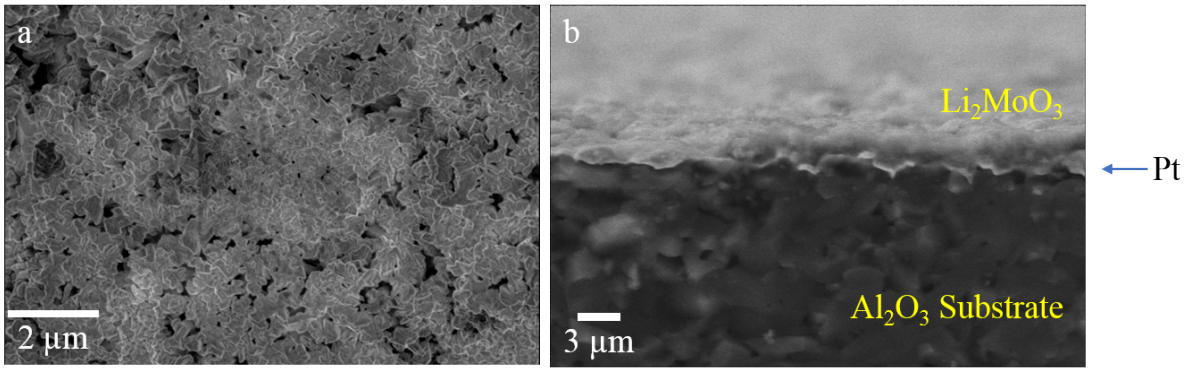

Figure 1. SEM images of the Li_2MoO_3 thin film cathodes showing (a) top surface morphology (collected at 1.00 kV) and (b) cross-sectional fracture surface (collected at 20.00 kV). A thin Pt layer (200 nm) was deposited on the Al_2O_3 substrate to serve as a current collector for electrochemical testing.

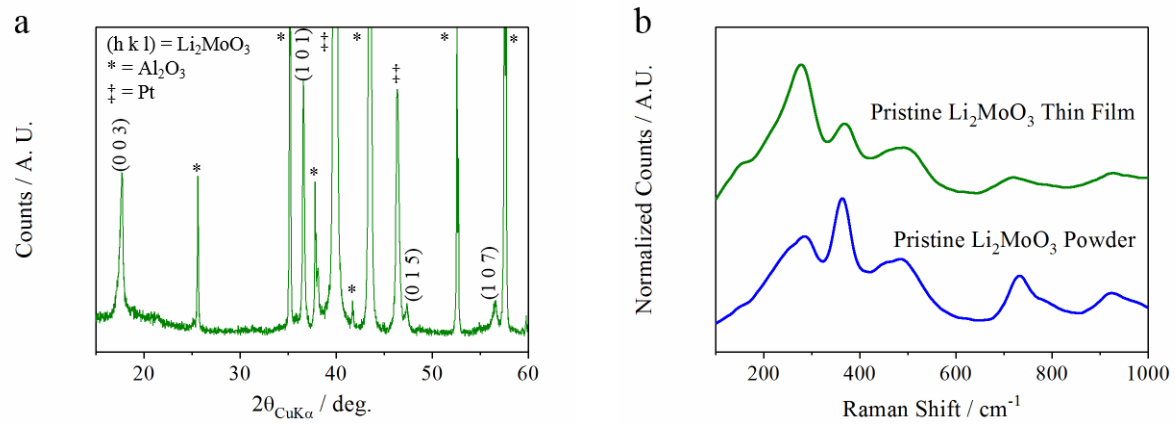

Figure 2. (a) XRD pattern collected for a Li_2MoO_3 thin film deposited on a Pt/Al_2O_3 substrate and (b) Raman spectra for a Li_2MoO_3 thin film and powder.

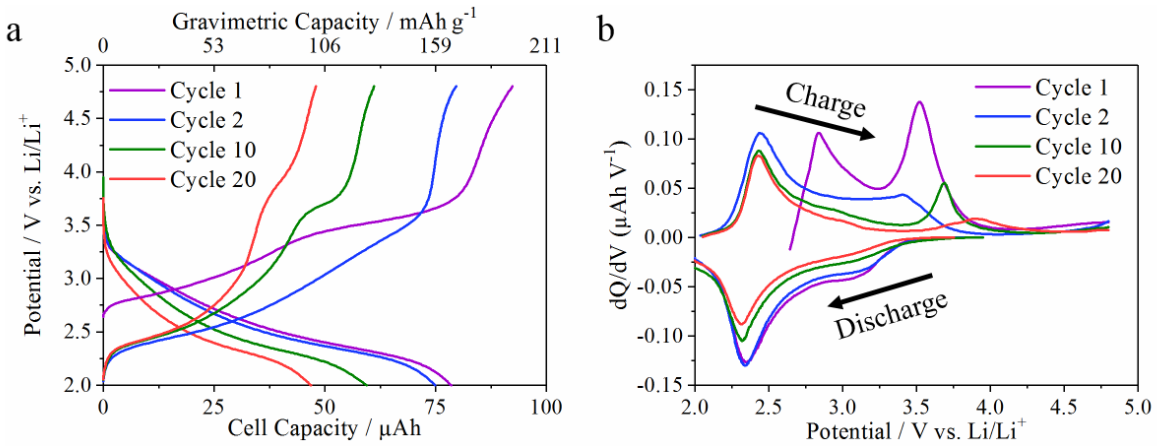

Figure 3. Half-cell electrochemical characterization of Li_2MoO_3 thin film cathodes cycled in a liquid carbonate electrolyte at room temperature. (a) Galvanostatic charge/discharge profiles and (b) differential capacity plots collected between 2.0 – 4.8 V vs. Li/Li^+ at a current density of 12 µA/cm^2.

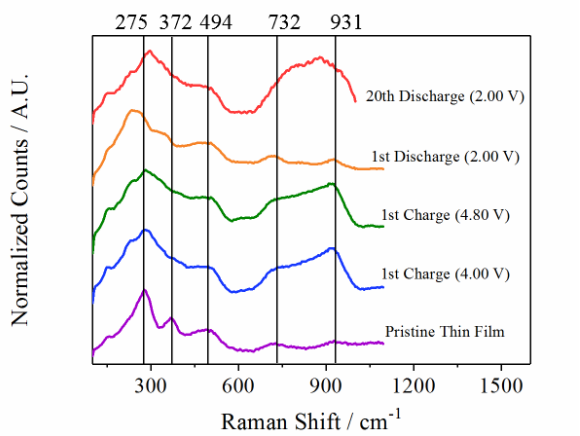

Figure 4. *Ex-situ* Raman spectra of thin film Li_2MoO_3 thin film cathodes at various states-of-charge during the first cycle and after 20 charge/discharge cycles. For cathodes harvested during the first cycle, the cells were galvanostatically charged/discharged to the desired cutoff potential at 12 µA/cm^2 followed by a 5 h hold at that potential. The sample harvested after 20 cycles was galvanostatically cycled between 2.0 – 4.8 V at 12 µA/cm^2 without any potential holds.

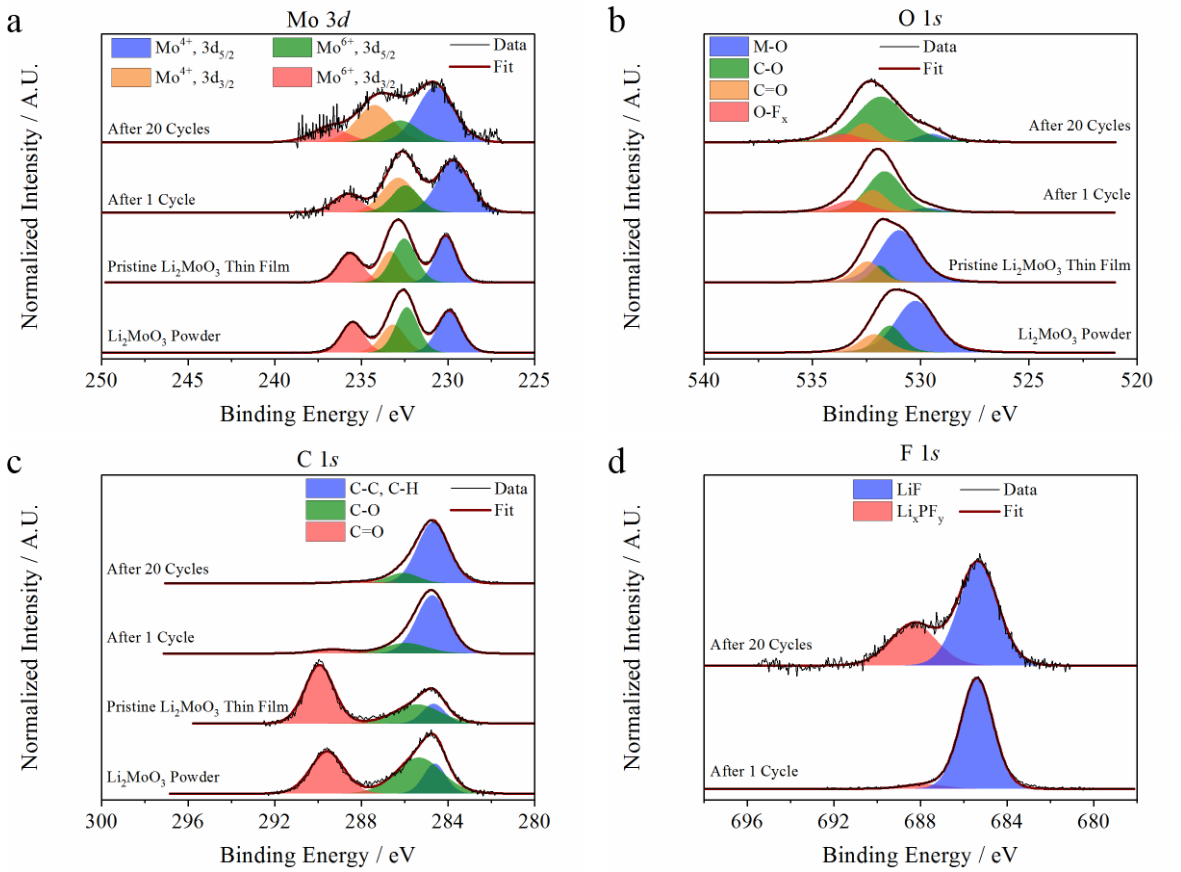

Figure 5. *Ex-situ* XPS spectra of pristine (i.e., uncycled) and cycled Li_2MoO_3 thin film cathodes collected after 1 and 20 charge/discharge cycles showing core-level scans for (a) Mo 3d, (b) O 1s, (c) C 1s, and (d) F 1s. Note that F 1s core level scans were not collected for the pristine samples.

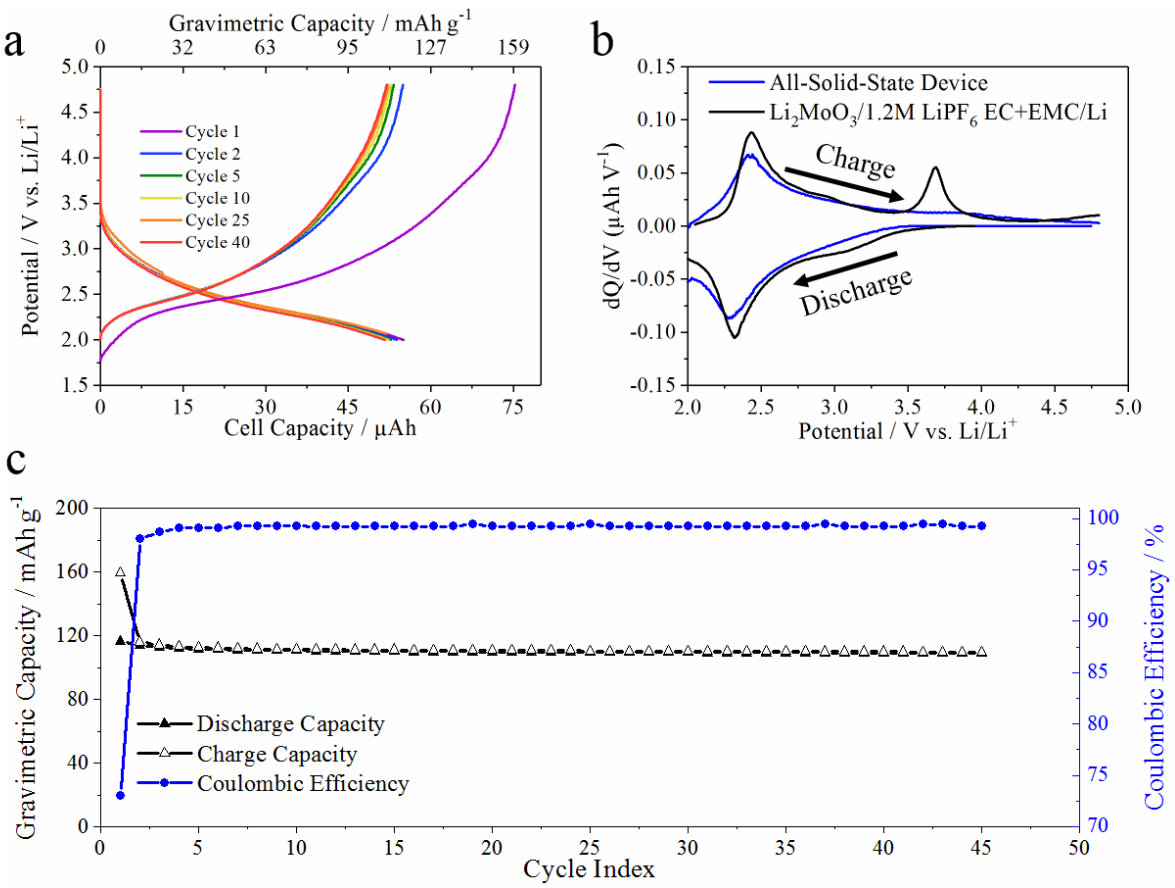

Figure 6. Electrochemical characterization of all-solid-state Li_2MoO_3/Lipon/Li batteries showing (a) galvanostatic charge/discharge profiles, (b) differential capacity plots, and (c) cycling stability collected between 2.0 – 4.8 V at a current density of 10 µA/cm^2 over 45 cycles at room temperature (ca. 23 °C). The differential capacity plot for the Li_2MoO_3/1.2M $LiPF_6$ EC+EMC/Li cell in (b) was acquired at a current density of 12 µA/cm^2 at room temperature.

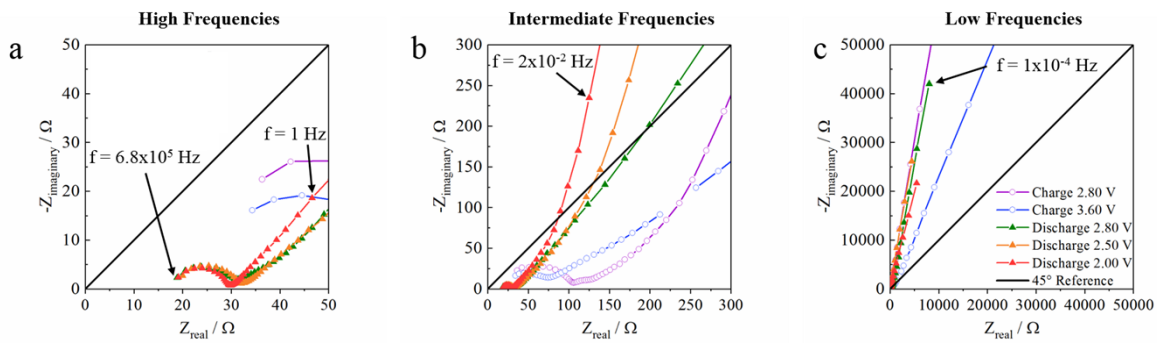

Figure 7. Nyquist plots for Li_2MoO_3/Lipon/Li thin film batteries collected at 80°C and at various states-of-charge. Panels (a-c) highlight the impedance at (a) high frequencies (f, up to 6.8x10^5 Hz), (b) intermediate frequencies, and (c) low frequencies (down to 1x10^{-4} Hz).

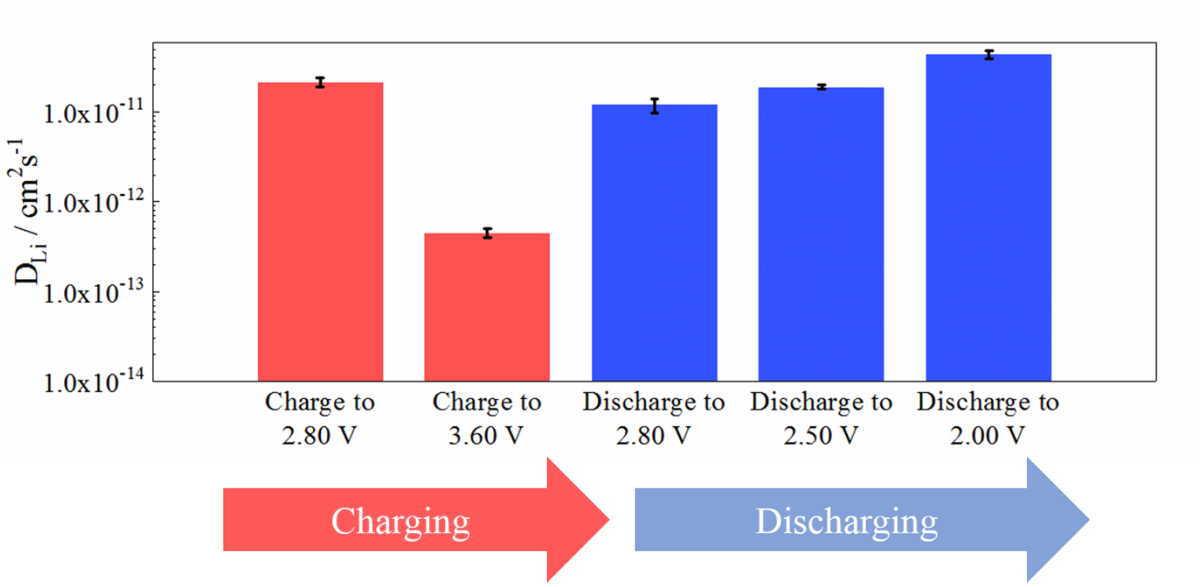

Figure 8. Li diffusion coefficients (D_{Li}) for Li_2MoO_3 thin film cathodes at 80°C at various states-of-charge as calculated using Equations 2 and 3. The error bars represent the range of diffusion coefficients determined from the slope of Z_{real} vs. $\omega^{-1/2}$ and $-Z_{imaginary}$ vs. $\omega^{-1/2}$ shown in Figure S1.